In situ Observation of Crystal Growth in a Basalt Melt and the Development of Crystal Size Distribution in Igneous Rocks

Huaiwei Ni[1,2], Hans Keppler[1], Nicolas Walte[1], Federica Schiavi[1,3], Yang Chen[4], Matteo Masotta[1], and Zhenjiang Li[2]

[1]*Bayerisches Geoinstitut, Universität Bayreuth, 95440 Bayreuth, Germany*

[2]*CAS Key Laboratory of Crust-Mantle Materials and Environments, School of Earth and Space Sciences, University of Science and Technology of China, Hefei 230026, China*

[3]*Laboratoire Magmas et Volcans, Université Blaise Pascal, 63038 Clermont-Ferrand, France*

[4]*Department of Earth and Environmental Sciences, The University of Michigan, Ann Arbor, MI 48109, USA*

27 pages (including this title page), 6767 words.

11 figures, 2 tables, supplementary material (3 figures, 4 movies).

Corresponding author:

Huaiwei Ni

E-mail: *hwni@ustc.edu.cn*

Tel. 86-551-63600297

Submitted to *Contributions to Mineralogy and Petrology* on Oct 20th, 2013

Resubmitted to *Contributions to Mineralogy and Petrology* on Mar 8th, 2014 after revision

Abstract

To understand the solidification processes of natural magma and the texture evolution of igneous rocks, we have carried out in situ observation of the crystallization of a high-K basaltic melt cooling from ~1240°C in a moissanite cell. In a series of experiments with different thermal history, olivine or clinopyroxene (cpx) appeared as the liquidus phase before the formation of plagioclase. During cooling at 100°C/hr, the morphology of olivine and cpx transited from tabular to hopper habit. To first order approximation, crystal grow rate (2×10^{-9} m/s to 7×10^{-9} m/s for olivine and 6×10^{-9} m/s to 17×10^{-9} m/s for cpx), probably limited by chemical diffusion, is proportional to crystal size. In one experiment dominated by olivine crystallization, the good image quality allows the analysis of texture evolution over an extended period. Nucleation of olivine occurred only in a narrow temperature and time interval below the liquidus. Two-dimensional length- and area-based crystal size distributions (CSDs) show counterclockwise rotation around axes of 8 μm and 100 μm^2, which is consistent with the proportionate crystal growth. Both CSDs and direct observation show the dissolution of small crystals and Ostwald ripening. These data suggest that conventional analyses of crystal size distributions of igneous rocks may be in error – the slope of the CSD cannot be interpreted in terms of a uniform growth rate and the intercept with the vertical axis does not correspond to a nucleation density.

Keywords: Crystal growth; crystal size distribution; basalt melt; igneous rocks

Introduction

Igneous rocks are formed by the solidification of silicate melts. The advance and disruption of solidification fronts in magmatic systems can have planetary-scale consequences, with the formation of the continental crust being one example (Marsh 2006). From a microscopic perspective, melt solidification is known to involve a series of physicochemical processes, including crystal nucleation, crystal growth, Ostwald ripening, and others. However, there is much to learn about the details, and in particular, about the mechanisms by which igneous texture evolves with cooling under the collective operation of these processes (Hersum and Marsh 2007). To tackle the inverse problem of deciphering magma history from rock texture, it is indispensable to obtain a good understanding of the forward solidification process (Hammer 2008).

Already Jambon et al. (1992) observed olivine growth in situ by heating basaltic melt inclusions trapped in plagioclase phenocrysts. However, the limited size of the melt inclusions (40-150 μm) precluded texture evolution from being traced. Immediately after its development (Schiavi et al. 2009), the moissanite cell (SiC single crystals being used as the window material) was recognized to be a useful tool for "capturing crystal growth" (Hammer 2009). The moissanite cell achieves better confined sample geometry and more precise temperature control than commonly used heating stages (e.g., Applegarth et al. 2013). In previous experiments carried out in the moissanite cell, quantitative texture analysis had been made on images collected from a supercooled melt at 900°C (Schiavi et al. 2009), but image quality was rather poor for experiments cooling from superliquidus temperatures such as 1250°C (Schiavi et al. 2010).

After technically improving the moissanite cell, we have been able to obtain continuous records of olivine, clinopyroxene and plagioclase crystallization in a high-K basaltic melt cooling from ~1240°C. Especially in one experiment, high-quality time-lapse images of olivine crystallization processes make it possible to trace not only the growth of individual crystals but also the texture evolution as represented by the crystal size distribution (CSD). These data allow current interpretations of the crystal size distribution in igneous rocks to be directly tested.

Experimental and analytical methods

Starting material

The starting material for in situ crystallization experiments was a synthetic basaltic glass with a composition targeted at the golden pumice PST-9 from the Stromboli volcano, Italy (Pichavant et al. 2011). Because the presence of iron would significantly degrade sample visibility in transmission under an optical microscope, FeO was substituted by an equal amount of MnO. Oxides and alkali nitrates were melted twice at 1500°C in a 1-bar chamber furnace, and the obtained glass was ground and melted again in a vacuum furnace to minimize the content of volatiles dissolved in the glass.

Schiavi et al. (2010) attributed bubble formation, which caused major problems in optical observation, to incomplete devolatization of their starting glass. We doubly polished the synthesized basaltic glass to wafers of ~50 μm thickness and analyzed their volatile contents with a Bruker IFS 120HR FTIR spectrometer in conjunction with a Bruker IRscope I. The FTIR spectrum (Online Resource Fig. A1) indicates that the CO_2 and H_2O contents of our basaltic glass cannot be higher than a few μg/g.

The amount of other volatiles (such as N_2) is expected to be even less because they are less soluble than CO_2 and H_2O. Compared with PST-9, our synthetic glass, free of visible bubbles or crystals, is slightly depleted in Ca and enriched in Si and alkalis (Table 1).

Moissanite cell experiments

The general design of the moissanite cell closely resembles that of a Bassett-type externally heated diamond anvil cell, adapted for higher temperature and ambient pressure. A detailed description of the first version of the moissanite cell can be found in Schiavi et al. (2009, 2010). Although a moissanite cell using 2 concentric coils of $Pt_{90}Rh_{10}$ heating wires per anvil in principle allowed heating up to 1250°C (Schiavi et al. 2010), heater breakage often occurred at high temperature. To solve this problem, we added a third $Pt_{90}Rh_{10}$ heating coil. This 3-coil setup (Online Resource Fig. A2) significantly enhanced the robustness of the heater and extended the lifetime of the moissanite cell. Furthermore, the glassy carbon gasket used in Schiavi et al. (2010), which was prone to oxidation despite flushing with an Ar–H_2 mixture, was replaced with an yttrium-stabilized zirconia gasket.

A glass chip of ~1.9 mm diameter and ~50 μm thickness was placed between the two moissanite anvils and observed in transmission with an optical microscope (Zeiss Axioscope 40; output to either eyepieces or camera-computer). The glass was first heated to 800°C (700°C for Run# Bas11) at a ramp rate of 1000°C/hr. The cell was then tightened and was allowed to relax at this temperature for several to a few tens of minutes, before further heating. To suppress crystallization and bubble formation during heating, temperature was rapidly increased to ~1240°C at 1×10^4 °C/hr (Fig. 1). Temperature was maintained at ~1240°C for several minutes, followed by cooling at

ramp rates of 50-2000 °C/hr to foster crystallization. At high temperature, the quality of sample image deteriorated with time. When the image became unsatisfactory, the experiment was quenched to ambient temperature at 1×10^4 °C/hr (2000 °C/hr for Run# Bas11).

Electron microprobe and SEM/EDS analyses

The chemical composition of the starting glass was analyzed by a JEOL JXA-8200 electron microprobe with a defocused beam of 15kV and 15 nA and 5 μm diameter. To examine chemical heterogeneity of the glass and minerals (olivine, clinopyroxene, and plagioclase) in the quenched products, a focused beam with the same acceleration voltage and current was used. Despite the employment of a special routine for Na analysis (by extrapolation to zero time photon counts), Na loss from the glass caused by the focused beam cannot be completely avoided. Backscattered electron (BSE) images of the quenched products were obtained with the electron microprobe and with an FEI scanning electron microscope (SEM), both of which were equipped with an energy-dispersive X-ray spectrometer (EDS) for phase identification.

Image analysis

Each sample image of 1600×1200 pixels (recorded under a 10× objective in transmission) corresponds to a visual field of 0.36 mm^2 (0.693 by 0.52 mm). Using the ImageJ64 program developed by the NIH, the length and width of tabular and hopper crystals were measured with an uncertainty of ~10% relative. Here we define 1D grain size to be the half length of the grain, with the "hopper" part counted for hopper crystals. In determining 2D crystal size distribution, the boundary of each crystal was hand redrawn to a closed polygon, the area of which was taken to be the

crystal size. Due to the overlap and clustering of crystals at different focal depths, known as the volume effect, a small amount of crystals without a well-defined boundary had to be excluded from the statistics.

Experimental results

In total eighteen crystallization experiments were carried out in the moissanite cell, among which four successful runs are reported here (Run# Bas11, Bas12, Bas14, and Bas21; Movies A1-A4 in Online Resource). Little change was observed in sample image during the first heating step and the dwell period at ~800°C, although we cannot rule out the possibility that some critical crystal clusters might have already developed at 800°C. In spite of the high ramp rate of the prime heating step (from 800°C to ~1240°C took only a few minutes), numerous crystals still appeared together with bubbles at ~1000°C, but the nucleated crystals were partly resorbed upon further temperature increase. Owing to the use of nearly volatile-free glass, the problem of bubbles degrading image quality was less severe than that observed in Schiavi et al. (2010).

Despite using the same starting glass in all the crystallization experiments, different minerals, as identified by EDS and electron microprobe analyses, formed in the four runs (Table 1). In Run# Bas11 (and Bas12), olivine was the dominant mineral; in Run# Bas14 and Bas21, clinopyroxene±plagioclase prevailed, with only some sporadic olivine crystals being present. Below, we will report the results from different experiments separately.

Olivine crystallization in Run# Bas11

The best visual record of olivine crystallization was obtained from an experiment (Run# Bas11; Movie A1) that encountered some technical problems. In this experiment, first signs of crystallization came into view at ~1048°C during heating (defined as $t = 0$), and there appeared to be a high nucleation density. After ~2 min dwell at ~1240°C, the $Pt_{90}Rh_{10}$ heater of the upper moissanite anvil failed. Nevertheless, the new 3-coil-heater setup allowed heating to be sustained by the heater of the lower anvil. During the subsequent cooling at 100°C/hr, the temperature reading of the upper thermocouple was below that of the lower one by about 100°C (Fig. 1). In the following, temperature will be referred to as the average of the two thermocouple readings.

Crystal morphology

Nucleation of new olivine crystals was observed only during a narrow temperature and time interval of a few minutes at the beginning of the experiment. During the subsequent cooling, only the growth of already existing crystals was observed, but not the appearance of new crystals. A similar confinement of nucleation to short events was also observed in other experiments.

At near-liquidus temperatures, olivine crystals moved and occasionally rotated in the melt, which is more close to natural conditions than the "staying in place" crystal growth in basaltic andesite at 900°C (i.e., crystals hardly moved once formed) in Schiavi et al. (2009). The apparent movement of the crystals was caused by the flow of the melt in response to the expansion, contraction or deformation of large gas bubbles, which can be clearly seen towards the end of Movie A1. Therefore, in reality, this was not so much a movement of individual crystals inside the melt, but a slight movement of the melt, which carried the crystals along.

In the first stage of cooling, such as at ~1142°C, most olivine crystals developed a tabular shape, while a limited number of them already grew "horns" along the long dimension, typically better developed at one end than the other (Fig. 2a). As temperature continued to decrease, a lot more crystals started to show hopper behavior, i.e., they developed an hourglass shape (Fig. 2b; Fig. 3a-e). According to Faure et al. (2003), the long dimension of tabular and hopper olivine crystals (Fig. 3a-o) corresponds to the [100] zone axis, and the short dimension corresponds to [001]. Although not particularly obvious in the time-lapse images, a quasi-hexagonal shape was found to be widespread in BSE images of the quenched sample (Fig. 4). The hexagonal shape is actually a sectioning effect of observing a hopper crystal along [100], and the "hollow" center of the hexagon corresponds to the cavity of a hopper crystal filled with melt/glass (Faure et al. 2003).

In some time-lapse images, we observed the presence of "ladder"-shaped hopper olivine crystals, with multiple melt inclusion cavities trapped in a single crystal (Fig. 3p-q). Up to eight inclusion cavities were distributed quite regularly along the [100] zone axis and were separated from each other by thin "bridges", apparently arising from repeated closing and reopening of hopper crystals to surrounding melt. Most cavities closed before the experiment ended, leaving just few, generally small inclusions in the quenched sample. The quenched sample also contains plenty of dendritic crystals, which judging from Movie A1 are probably clinopyroxene nucleated during the dwell at ~900°C.

While most crystals continued to grow over the entire span of the experiment, some crystals with size less than 6 μm, with one example shown in Fig. 5, appeared to shrink following a brief stage of growth. Simultaneous growth of big crystals and dissolution of small ones suggests the occurrence of Ostwald ripening.

Crystal growth rates

The traditional "snapshot" technique used in quench experiments evaluates crystal growth rate from the change of average size of many crystals (Hammer 2008), which relies on statistics and hence involves extra uncertainty. In contrast, our in situ observation permits to trace the growth of individual crystals (Fig. 3a-o; Fig. 6a). These data further allow to directly test whether crystal growth rate is uniform, as often assumed (e.g., Marsh 1988), or whether it depends on crystal size (Eberl et al. 2002; Kile and Eberl 2003).

From the growth curves of eight olivine crystals in Fig. 6a, t = 34 min, at which all the considered crystals still enjoyed free growth (i.e., no impingement by surrounding crystals), was chosen to be an appropriate moment for comparing growth rates, calculated using a central differential algorithm. The growth rates of olivine, with an estimated uncertainty of 20%, fell within 2×10^{-9} m/s to 7×10^{-9} m/s (Fig. 6b). While decreasing temperature did not appear to modify the slope of growth curve significantly even across the tabular-hopper transition (Fig. 6a), there is a general positive correlation between growth rate and crystal size (Fig. 6b) – larger crystals tended to grow more rapidly than smaller ones, in contrast with some previous results (e.g., Applegarth et al. 2013). To first order approximation, olivine growth rate is roughly proportional to crystal size. For a given crystal, the rate of lateral growth (growth along [001]) was smaller than longitudinal growth rate by a factor of ~3, but larger crystals were also found to grow faster laterally than smaller crystals.

Development of crystal size distribution

The crystal size distribution (CSD) theory, since developed by Marsh (1988, 1998), has been widely used for quantitative description and interpretation of rock texture (Armienti 2008). With our in situ technique, texture evolution of the melt can be conveniently followed. Two-dimensional olivine CSDs of 5 snapshots taken during cooling were carefully measured using 5 logarithmic size bins (Table 2), according to either half length along [100] (Fig. 7a) or crystal area (Fig. 7b). The plotted CSDs are roughly log-linear except the first one or two logarithmic size bins, similar to the plagioclase CSDs in Schiavi et al. (2009). For both length- and area-based analyses, we observe a counterclockwise rotation of CSD, around axes of 8 μm and 100 μm^2, respectively. The population densities of crystals larger than these threshold values increased with time, whereas those of small crystals continued to decrease.

Composition of olivine and melt

The average composition of olivine in the quenched product (Table 1) can be given as $(Mg_{0.838}Mn_{0.153}Ca_{0.009})_2SiO_4$. Due to olivine crystallization, in far-field melt (i.e., melt at some distance away from olivine crystals), the contents of oxide components other than MgO and MnO became higher than in the starting glass (Table 1). A simple mass balance calculation indicates that olivine crystals sum to approximately 12 wt% in the quenched sample, which translates to ~10.7% modal abundance for olivine considering the density difference between olivine and melt/glass. The only mismatch between the bulk composition of the quenched product as (12 wt% olivine+88 wt% glass) and that of the starting glass is in terms of Na_2O content (Table 1), which is attributed to Na loss by the focused beam used in microprobe analysis on the quenched glass, although minor Na loss may also have occurred during the experiment.

Clinopyroxene and plagioclase crystallization

Unlike in Bas11, clinopyroxene (cpx) was the dominant liquidus phase in Bas14 (Movie A3; Fig. 8a) and Bas21 (Movie A4; Fig. 8b-c). In Bas14, during cooling at 100°C/hr, cpx first appeared at ~1212°C in the form of tabular crystals. Similar to olivine in Bas11, from ~1189°C cpx started to develop a hopper behavior, which was preserved in the quenched Bas14 sample (Fig. 8a). Furthermore, the growth rate of cpx crystals also depended on crystallographic orientation, and more importantly, on crystal size. Again, the longitudinal growth rate, ranging from 6×10^{-9} m/s to 17×10^{-9} m/s at 1192°C, is approximately proportional to crystal size (Fig. 9). Therefore, proportionate growth appears to be ubiquitous for the crystallization of minerals from magma.

In Bas21, nuclei of cpx crystals already existed at 1240°C. They continued to grow during cooling to 1150°C at 2000°C/hr. During the dwell at 1150°C, plagioclase crystals grew rapidly from several nucleation points in a radiating manner, and the mechanical interference with plagioclase broke the earlier formed cpx crystals into pieces (Fig. 10), which was consistent with the texture of the quenched sample (Fig. 8b-c). In agreement with our observations, cooling to 1100°C of a shoshonitic melt (compositionally similar to PST-9) at 900 °C/h produced intergrowths of plagioclase and clinopyroxene with skeletal and hopper shapes (Conte et al. 2006). No dendritic crystals were found in the quenched samples of Bas14 and Bas21 as those in Bas 11 (Fig. 4), which was probably due to the higher quenching rates in the former two runs.

The cpx in Bas21 has a higher Mn/Mg ratio than that in Bas14 (Table 1). In both experiments only a small amount of olivine crystals were found in the quenched

samples (shown in Fig. 8a for Bas14). The olivine in Bas14 is compositionally similar to that in Bas11, but the olivine crystals in Bas21 have a much higher Mn/Mg ratio, indicating that the latter formed in a much later stage than cpx (from an Mn-enriched melt). This is coherent with the rapid cooling from 1240°C to 1150°C in Bas21 – according to Donaldson (1979), the delay in olivine nucleation in basaltic liquids increases with the increase of cooling rate.

The image quality of Bas14 and Bas21 is inferior to that of Bas11, and hence does not allow a reliable texture analysis to be made.

Discussion

Mineralogical differences between the experiments

For a synthetic melt compositionally similar to PST-9, Pichavant et al. (2009) found that during cooling at ambient pressure, olivine and clinopyroxene appeared at 1190°C and plagioclase formed at 1180°C. For our basaltic composition, the MELTS program (Ghiorso and Sack 1995) predicts that olivine $(Mg_{0.84}Mn_{0.15}Ca_{0.01})_2SiO_4$ should appear at 1218°C and 0.1 MPa as the liquidus phase. Because the same starting glass was used in all the crystallization experiments, the different mineralogy, predominantly olivine in Bas11 and Bas12 and cpx±plagioclase in Bas14 and Bas21, must seek an explanation from kinetics considerations. In view of the proximity of crystallization temperatures of the three minerals (Pichavant et al. 2009), we suggest that subtle changes in the initial heating and cooling paths may be sufficient for causing the nucleation of different minerals. During the subsequent cooling, the phase that nucleated first may deplete the melt in Mg and therefore suppress the nucleation of the second phase. For Bas11, we highlight the excellent agreement

between the olivine composition [$(Mg_{0.838}Mn_{0.153}Ca_{0.009})_2SiO_4$] and the prediction of MELTS.

Mechanisms and rates of olivine growth in Bas11

In their dynamic crystallization experiments with a synthetic CaO-MgO-Al_2O_3-SiO_2 basalt, Faure et al. (2003) found that for cooling rates in the range of 50-200°C/hr, hopper crystals were the dominant olivine morphology for 50-200°C undercooling. Our in-situ observations are entirely consistent with their results obtained using the traditional technique, as well as with the in situ observation of melt inclusion by Jambon et al. (1992).

Different mechanisms for crystal growth from silicate melts have been proposed by a number of authors (e.g., Kirkpatrick 1975; Sunagawa 2005; Faure et al. 2007). At low degree of undercooling ΔT, spiral growth (by a screw dislocation mechanism) is taking place, crystal surfaces are smooth, and crystals typically exhibit a polyhedral/tabular morphology. At intermediate degree of undercooling, layer-by-layer growth (or called two-dimensional nucleation) dominates, crystal surfaces roughen, and hopper crystals are prevalent. At large undercooling, it transits to adhesive-type continuous growth, and dendritic or swallowtail crystals form. With respect to the formation of tabular and hopper olivine crystals in Bas11, both spiral growth and layer-by-layer growth must have been operative.

However, this does not mean that the growth rate of olivine is controlled by these interface reaction mechanisms. For olivine growth in the basalt melt, MgO and MnO need to be carried from far-field melt to olivine-melt interfaces, and incompatible components such as Al_2O_3 need to be transported away. Concentration gradients of these oxide components were found in the melt close to olivine-melt interface along

both [100] and [001] (Online Resource Fig. A3), generally consistent with the observations of Faure and Schiano (2005) except for CaO. The flat Na_2O profile is probably due to fast Na diffusion. The presence of concentration gradients strongly suggests that mass transfer played a crucial role in limiting crystal growth rate (Zhang 2008). In view of the small change in olivine growth rate across the tabular-hopper transition (Fig. 6a), we suggest that chemical transport, rather than interface reaction, perhaps already controlled olivine growth from early on. This is also consistent with the previous finding of olivine growth rate peaking at ~20 K undercooling (Lasaga 1998).

MgO was identified by Chen and Zhang (2008) to be the principal equilibrium-determining component for transport-controlled olivine dissolution or growth in basaltic melt. In diffusive crystal dissolution or growth, the dissolution/growth rate may be estimated by $\alpha(\rho^m/\rho^c)(D/t)^{1/2}$, with α being a dimensionless parameter depending on interface composition, ρ^m and ρ^c being the density of the melt and that of the crystal, D being MgO diffusivity and t being time. Here it is difficult to constrain α accurately, but 0.03 may be a reasonable value (e.g., Zhang 2008). For a characteristic t of 900 s (cooling by 50°C) and $D_{MgO} \sim 10^{-12}$ m^2/s at 1150-1050°C (Chen and Zhang 2008), crystal growth rate under our experimental conditions should be around 10^{-9} m/s, which is lower than but roughly consistent with the measured grow rates (Fig. 6b). The difference may be attributed to growth aided by the movement of crystals in the melt.

While chemical diffusion is recognized to be a determinative mechanism in limiting olivine growth, it is certainly not the *only* operative mechanism – otherwise olivine crystals should grow into spheres. The difference between the growth rate along [100] and that along [001] must arise from different interface reaction rates. It

is still not clear which mechanism may account for size-dependent growth rate, but a close link between proportionate growth and transport-controlled growth has already been realized (Eberl et al. 2002).

Closed hopper olivine crystals and melt convection

We observed in Bas11 the presence of closed hopper olivine crystals with multiple melt inclusions (Fig. 3p-q). Inside pumice samples from Stromboli volcano, euhedral olivine crystals were found to coexist with melt inclusion-bearing hollow (hopper) crystals and closed skeletal olivines, sometimes exhibiting dendritic overgrowths (Métrich et al. 2010). The correspondence between experimental and natural textures thus highlights that crystal morphologies and quantities of entrapped melts are important parameters carrying information on the cooling history of the magma.

Closed hopper olivine crystals in basalts dredged from the Mid-Atlantic Ridge were attributed to turbulent convection beneath the ridge and the experience of several cooling-heating cycles (Faure and Schiano 2004; Welsch et al. 2009; Colin et al. 2012). Since there was a thermal gradient in Bas11, one may expect that the formation of closed hopper crystals in Bas11 also arose from melt convection. However, several lines of evidence suggest the absence of convection during the experiment. Firstly, the movement of crystals was largely horizontal; otherwise a change of focal depth of the crystals would have been observed. In another experiment Bas12 (Movie A2) that did not involve a thermal gradient, melt and crystals moved much more dynamically (the boiling finally caused most melt to be lost). Furthermore, for melt convection to occur would require a high Rayleigh number, which is calculated as $(\rho g \alpha \Delta T L^3)/\eta\kappa$ with ρ being melt density, g being the gravitational acceleration, α being thermal expansivity, ΔT being temperature

difference, L being characteristic length scale, η being melt viscosity, and κ being thermal diffusivity. For the melt at 1373-1473 K in Bas 11, assuming 2.6×10^3 kg/m^3 for density and 5×10^{-5} /K for thermal expansivity (Lange and Carmichael 1987), 100 K for the maximum temperature difference over the 5×10^{-5} m melt thickness, 1×10^3-1×10^4 Pa s for viscosity (Hui and Zhang 2007), and 3×10^{-7} m^2/s for thermal diffusivity (Nabelek et al. 2012), the Rayleigh number of the system is estimated to be only 5×10^{-9} to 5×10^{-8}, more than 10 orders of magnitude below the value ($> 10^3$) required for convection. Therefore, repeated cooling and heating may not be necessary for developing the complex morphology of closed hopper crystals.

Physical processes shaping CSD

The volume effect due to crystals aggregating and overlapping inevitably affected the accuracy of texture analysis of Bas11. However, the uncertainty caused by the volume effect is inferred to be insignificant. As shown in Table 2, the modal abundance of olivine increased with time, and reached ~10.5% for the last snapshot. This value is in good agreement with the 10.7% inferred from chemical analysis, and suggests limited counting errors from neglecting crystal clots. Decreasing crystal density (Table 2) was most likely caused by physical processes such as crystal coalescence (e.g., Schiavi et al. 2009) and Ostwald ripening. Ostwald ripening involves negative growth and elimination of small crystals (Fig. 5), consistent with evolution of the population density of the first two logarithmic size bins (Fig. 7).

Many applications of the crystal size distribution theory (Marsh 1988, 1998) assumed that (1) Nucleation rate and nucleation density increase exponentially with time and undercooling and (2) the rate of crystal growth is constant and uniform for all crystals. If these two assumptions were correct, CSD should be shifted parallel to

itself upon progressive crystallization. However, neither the assumptions nor the inferred CSD evolution agrees with our observations. Results from this study show conclusively that (1) nucleation of olivine or cpx occurred only in a narrow time and temperature interval at the beginning of the experiment; (2) growth rate was not uniform; rather, growth was roughly proportionate, i.e., the larger the crystal the higher the growth rate (Figs. 6b and 9b); and (3) CSD rotated counterclockwise with time (Fig. 7).

Nucleation and crystal growth are two competing mechanisms that both will reduce the supersaturation of the melt (Toramaru 1991). In general, crystal nucleation requires a larger degree of undercooling or supersaturation than crystal growth (e.g., Zhang 2008), as in a nucleus, the ratio of surface to volume is high so that the higher surface energy will counteract the free energy change of crystallization. Therefore, as soon as some olivine nuclei have formed, the growth of these crystals removes olivine component from the melt and suppresses further nucleation and the crystallization of other minerals such as cpx. Nucleation therefore stops once a first generation of olivine nuclei starts growing. Proportionate growth, with growth rates increasing with crystal size, has been observed in various systems (Kile and Eberl 2003 and references therein). Kile and Eberl (2003) presented evidence that proportionate growth is expected to occur whenever advection supplies material to the surface of crystals. This again is consistent with our experimental results, as crystals moved horizontally in the melt and as the growth rate predicted from diffusion alone is somewhat smaller than measured growth rates.

As shown in Fig. 11, proportionate growth will naturally cause the CSD slope to decrease. In the absence of new nucleation, the intercept of CSD with the vertical axis has to decrease, for the total number of crystals to be conserved. The reduction

in both slope and intercept leads to a counterclockwise rotation of the CSD (Fig. 11). On top of that, small crystals may partly or completely dissolve due to their higher surface energies (their negative growth rates are qualitatively consistent with proportionate growth), which cause their population density to fall below the log-linear CSD curve (Fig. 11) and the total number of crystals to decrease (Table 2).

Concluding remarks

In this study, we directly observed the transition of olivine and cpx morphology from tabular to hopper habit (Fig. 2; Fig. 3a-e; Movie A1 and A3), the incorporation of melt inclusions in closed hopper olivine crystals (Fig. 3p-q), and the dissolution of small olivine crystals (Fig. 5). Spiral growth and layer-by-layer growth are inferred to be the mechanisms for interface reaction, but the growth rate, varying with crystal size and crystallographic orientation, was primarily limited by chemical diffusion (helped by advection). The formation of closed hopper crystals may not necessarily require a complex thermal history.

The most important result of this study, however, is that it provides a new interpretation of the CSDs observed in igneous rocks. Our data suggest that during cooling of a magma, short nucleation events occur that generate an initial, log-linear CSD. The log-linear shape of this curve may indeed reflect an exponential increase of nucleation rate with time and undercooling, as often assumed in crystal size distribution theory. However, these events are short and nucleation does not continue during the growth of crystals. Rather, as soon as some crystals start to grow, they reduce the oversaturation that would be required for further nucleation and thus nucleation essentially stops. The further development of CSD is exclusively due to the growth of the initially established ensemble of nuclei. Proportionate growth in

conjunction with the negative growth of small crystals causes counterclockwise CSD rotation and a decrease in the population density of small crystals and in the total number of crystals.

The traditional interpretation of CSDs of igneous rocks may therefore be fundamentally flawed. The slope does not give an average growth rate. Rather, even if growth rate does not depend on time, the CSD rotates and becomes flatter due to the increase of growth rate with crystal size. The slope of the CSD is therefore primarily controlled by time and the *difference* in growth rates between the smallest and largest crystals, rather than by average growth rate. Similarly, the intercept of the CSD with the vertical axis does not give a nucleation density; rather, it gives a *lower limit of the initial nucleation density*, because of both proportionate growth and the elimination of small crystals by Ostwald ripening. More generally, the idea behind classical CSD theory that nucleation and crystal growth occur simultaneously over a large temperature and time interval does not capture the reality of nature. In reality, nucleation of each mineral is probably limited to a short event, which is followed by a long period of crystal growth and annealing. When multiple nucleation events occur during magma storage and ascent (e.g., Armienti et al. 1994), these events are likely related to rapid perturbations in pressure and temperature.

Acknowledgements

We thank Hubert Schulze and Raphael Njul for sample preparation, Sven Linhardt for technical assistance, Ulrike Trenz, Yuan Li and Mattia Giannini for SEM and EMPA analyses, and Julia Hammer and an anonymous reviewer for constructive reviews. Discussion with Andreas Audétat and Youxue Zhang was beneficial. This work was supported by the visitor program of Bayerisches Geoinstitut, Germany, the 111

Project of Ministry of Education, China, the Recruitment Program of Global Experts (Thousand Talents), China and the Natural Science Foundation of China (41322015).

References

Applegarth LJ, Tuffen H, James MR, Pinkerton H, Cashman KV (2013) Direct observations of degassing-induced crystallization in basalts. Geology 41:243-246.

Armienti P (2008) Decryption of igneous rock textures: crystal size distribution tools. Rev Mineral Geochem 69:623-649.

Armienti P, Pareschi MT, Innocenti F, Pompilio M (1994) Effects of magma storage an ascent on the kinetics of crystal growth. Contrib Mineral Petrol 115:402-414.

Chen Y, Zhang Y (2008) Olivine dissolution in basaltic melt. Geochim Cosmochim Acta 72:4756-4777.

Colin A, Faure F, Burnard P (2012) Timescales of convection in magma chambers below the Mid-Atlantic ridge from melt inclusions investigations. Contrib Mineral Petrol 164:677-691.

Conte AM, Perinelli C, Trigila R (2006) Cooling kinetics experiments on different Stromboli lavas: effects on crystal morphologies and phase composition. J Volcanol Geotherm Res 155:179-200.

Donaldson CH (1979) An experimental investigation of the delay in nucleation of olivine in mafic magmas. Contrib Mineral Petrol 69:21-32.

Eberl DD, Kile DE, Drits CA (2002) On geological interpretations of crystal size distributions: constant vs. proportionate growth. Am Mineral 87:1235-1241.

Faure F, Trolliard G, Nicollet C, Montel J-M (2003) A development model of olivine morphology as a function of the cooling rate and the degree of undercooling. Contrib Mineral Petrol 145:251-263.

Faure F, Schiano P (2004) Crystal morphologies in pillow basalts: implications for mid-ocean ridge processes. Earth Planet Sci Lett 220:331-344.

Faure F, Schiano P (2005) Experimental investigation of equilibration conditions during forsterite growth and melt inclusion formation. Earth Planet Sci Lett 236:882-898.

Faure F, Schiano P, Trolliard G, Nicollet C, Soulestin B (2007) Textural evolution of polyhedral olivine experiencing rapid cooling rates. Contrib Mineral Petrol 153:405-416.

Ghiorso MS, Sack RO (1995) Chemical mass transfer in magmatic processes IV. A revised and internally consistent thermodynamic model for the interpolation and extrapolation of liquid-solid equilibria in magmatic systems at elevated temperatures and pressures. Contrib Mineral Petrol 119:197-212.

Hammer JE (2008) Experimental studies of the kinetics and energetics of magma crystallization. Rev Mineral Geochem 69:9-59.

Hammer JE (2009) Capturing crystal growth. Geology 37: 1055-1056.

Hersum TG, Marsh BD (2007) Igneous textures: on the kinetics behind the words. Elements 3:247-252.

Hui H, Zhang Y (2007) Toward a general viscosity equation for natural anhydrous and hydrous silicate melts. Geochim Cosmochim Acta 71:403-416.

Jambon A, Lussiez P, Clocchiatti R, Weisz J, Hernandez J (1992) Olivine growth rates in a tholeiitic basalt: an experimental study of melt inclusions in plagioclase. Chem Geol 96:277-287.

Kile DE, Eberl DD (2003) On the origin of size-dependent and size-independent crystal growth: influence of advection and diffusion. Am Mineral 88:1514-1521.

Kirkpatrick RJ (1975) Crystal growth from the melt: a review. Am Mineral 60:798-814.

Lasaga AC (1998) Kinetic Theory in the Earth Sciences. Princeton, New Jersey, Princeton University Press, 581-712p.

Lange RA, Carmichael ISE (1987) Densities of Na_2O-K_2O- CaO-MgO-FeO-Fe_2O_3-Al_2O_3-TiO_2-SiO_2 liquids: new measurements and derived partial molar properties. Geochim Cosmochim Acta 51:2931-2946.

Marsh BD (1988) Crystal size distribution (CSD) in rocks and the kinetics and dyanamics of crystallization. I. Theory. Contrib Mineral Petrol 99:277-291.

Marsh BD (1998) On the interpretation of crystal size distributions in magmatic systems. J Petrol 39:553-599.

Marsh BD (2006) Dynamics of magmatic systems. Elements 2:287-292.

Métrich N, Bertagnini A, Di Muro A (2010) Conditions of magma storage, degassing and ascent at Stromboli: new insights into the volcano plumbing system with inferences on the eruptive dynamics. J Petrol 51:603-626.

Nabelek PI, Hofmeister AM, Whittington AG (2012) The influence of temperature-dependent thermal diffusivity on the conductive cooling rates of plutons and temperature-time paths in contact aureoles. Earth Planet Sci Lett 317-318:157-164.

Pichavant M, Di Carlo I, Le Gac Y, Rotolo SG, Scaillet B (2009) Experimental constraints on the deep magma feeding system at Stromboli volcano, Italy. J Petrol 50:601-624.

Pichavant M, Prompilio M, D'Oriano C, Di Carlo I (2011) Petrography, mineralogy and geochemistry of a primitive pumice from Stromboli: implications for the deep feeding system. Eur J Mineral 23:499-517.

Schiavi F, Walte N, Keppler H (2009) First in situ observation of crystallization processes in a basaltic-andesitic melt with the moissanite cell. Geology 37:963-966.

Schiavi F, Walte N, Konschak A, Keppler H (2010) A moissanite cell apparatus for optical in situ observation of crystallizing melts at high temperature. Am Mineral 95:1069-1079.

Sunagawa I (2005) Crystals: Growth, Morphology and Perfection. Cambridge, UK, Cambridge University Press, 45-53p.

Toramaru A (1991) Model of nucleation and growth of crystals in cooling magmas. Contrib Mineral Petrol 108:106-117.

Welsch B, Faure F, Famin V, Bachelery P, Famin V (2009) Microcrysts record transient convection at Piton de la Fournaise Volcano (La Reunion Hotspot). J Petrol 50:2287-2305.

Zhang Y (2008) Geochemical Kinetics. Princeton, New Jersey, Princeton University Press, 47-54p.

FIGURE CAPTIONS

Fig. 1 Thermal history of four moissanite cell experiments (Run# Bas11, Bas12, Bas14, and Bas21). In Bas11, olivine nucleation appeared at 1048°C (solid circle, defined as t =0); failure of the upper heater caused temperature reading of the upper thermocouple (11U) to be smaller than that of the lower thermocouple (11L) by ~100°C during cooling, with their average shown in curve "Bas11". On this curve, the moments for the two snapshots in Fig. 2 are shown in triangles, and those for the crystal "A" in Fig. 3 are shown in open circles. The curves for other runs are horizontally offset for clarity, and the time or t referred to in the text and other figures is invariably consistent with Fig. 1.

Fig. 2 Real-time photomicrographs of olivine crystals in basaltic melt cooling at 100°C/hr in Bas11. (a) T ~1142°C; most olivine crystals showed a tabular habit with some exceptions (two examples are circled with ellipse); (b) T ~1062°C; numerous hopper crystals formed. Crystal "A" (see Fig. 3 and Fig. 6) is enclosed with rectangle in both (a) and (b).

Fig. 3 Evolution of individual olivine crystals at size-dependent growth rates in Bas11: (a-e) Crystal "A", fast growth and transition from tabular shape to hopper shape; (f-j) Crystal "B", with an intermediate growth rate; (k-o) Crystal "C", slow growth; (p-q) two closed hopper crystals trapping multiple melt inclusions.

Fig. 4 (a) Zoom-out and (b) close-up BSE images of quenched Bas11 sample. Zone axes of olivine crystals are indicated in (b). The dendrites are presumably clinopyroxene crystals formed during the dwell at ~900°C.

Fig. 5 Dissolution of a small olivine crystal in Bas11, being circled with ellipse in the top panel (at t = 34 min or 12:00:00 in Movie A1).

Fig. 6 (a) Growth of half length along [100] for eight olivine crystals in Bas11. For crystals "A", "D", and "E", the crystal shape transition (from tabular to hopper shape) is indicated by a break in the curve. For crystals "B", "F", and "G", a conspicuous slow down is attributed to the impingement by surrounding crystals. (b) Growth rate at t = 34 min is roughly proportional to crystal size. Error bars represent ±20% uncertainty.

Fig. 7 Counterclockwise rotation of two-dimensional crystal size distributions (CSDs) during cooling in Bas11, according to (a) half length along [100]; and (b) crystal area.

Fig. 8 BSE images of quenched samples (a) Bas14; and (b)&(c) Bas21. In Bas14, Hopper clinopyroxene (cpx) crystals formed the dominant mineral phase, with some sporadic olivine (ol) cyrstals. In Bas21, cpx crystals were often broken into pieces by the later formed plagioclase (plag).

Fig. 9 (a) Half length of five clinopyroxene crystals in Bas14. For crystals "C" and "E", the tabular to hopper transition is indicated by a break in the curve. (b) Size-dependent clinopyroxene growth rate at t = 48.6 min. Error bars represent ±20% uncertainty.

Fig. 10 Real-time photomicrographs of Bas21 showing the disruption of cpx crystals by plagioclase (dark root and limbs) at 1150°C.

Fig. 11 Interpretation of the observed CSD evolution. A short nucleation event produces an initial CSD (thin solid line). Due to proportionate growth (rightward horizontal arrows) and conservation of the number of crystals, CSD evolves into the thick solid line. In addition, Ostwald ripening acts to reduce the population density and size of small crystals.

Figure1
Click here to download high resolution image

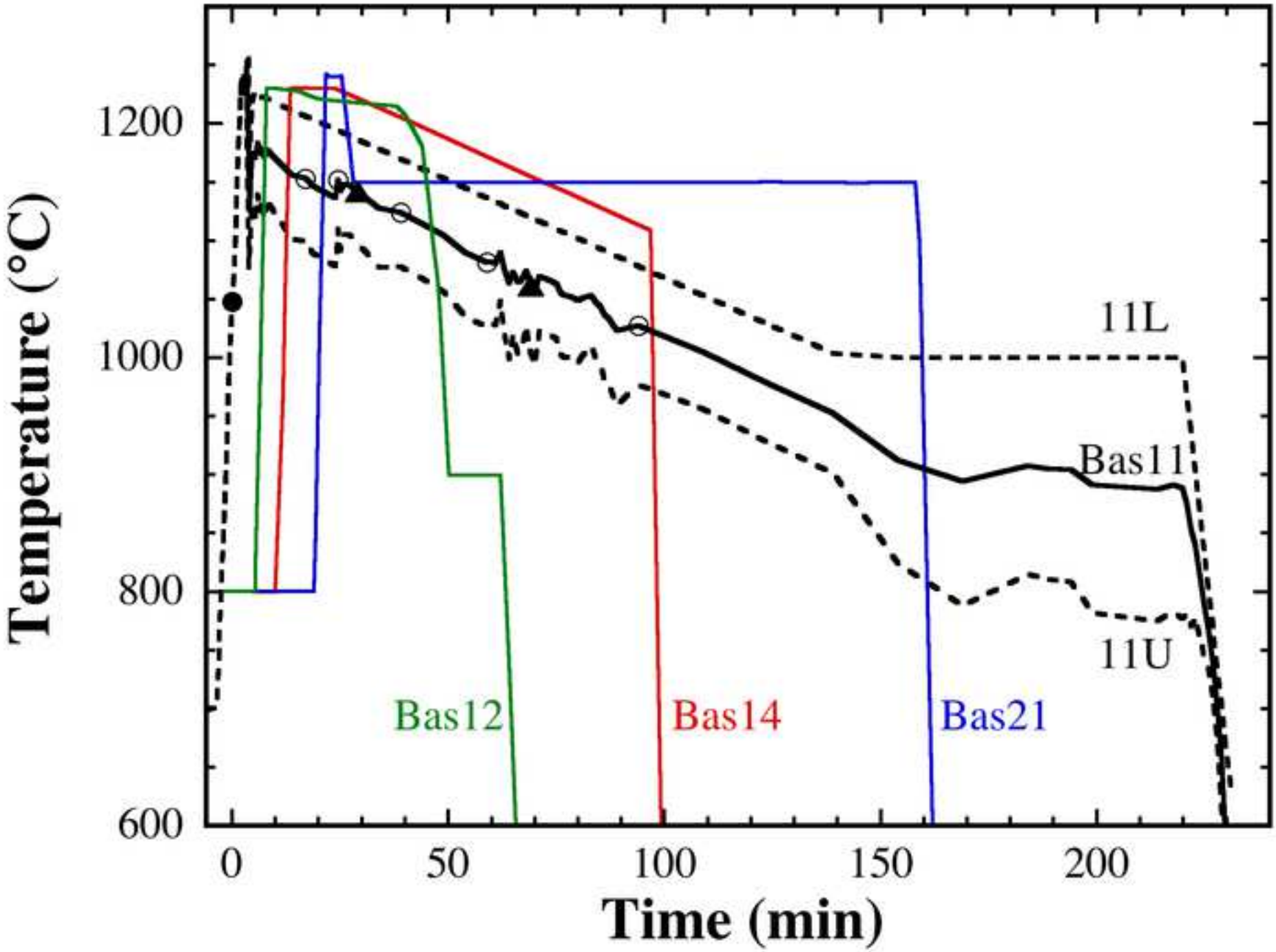

Figure2
Click here to download high resolution image

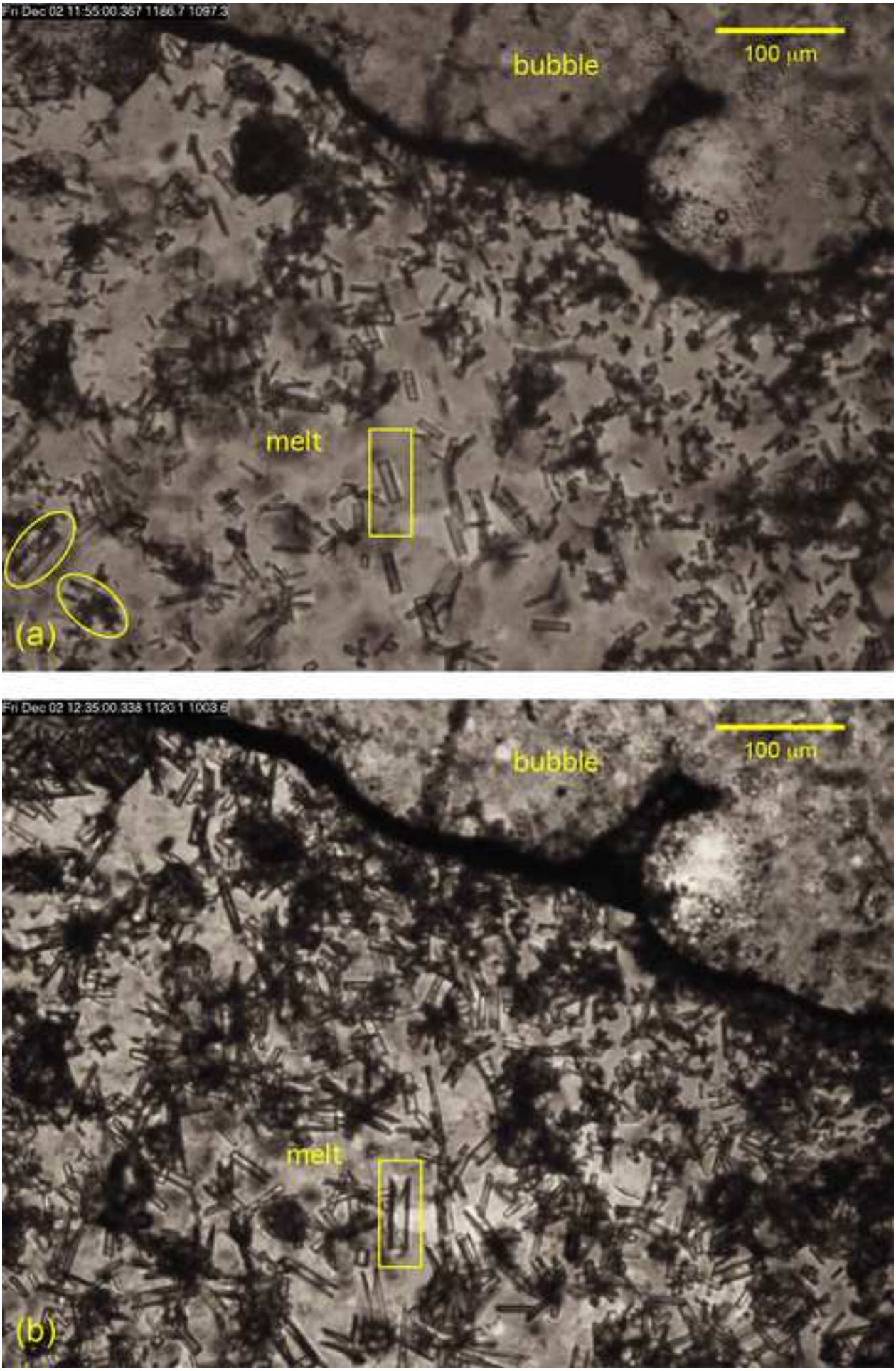

Figure3
Click here to download high resolution image

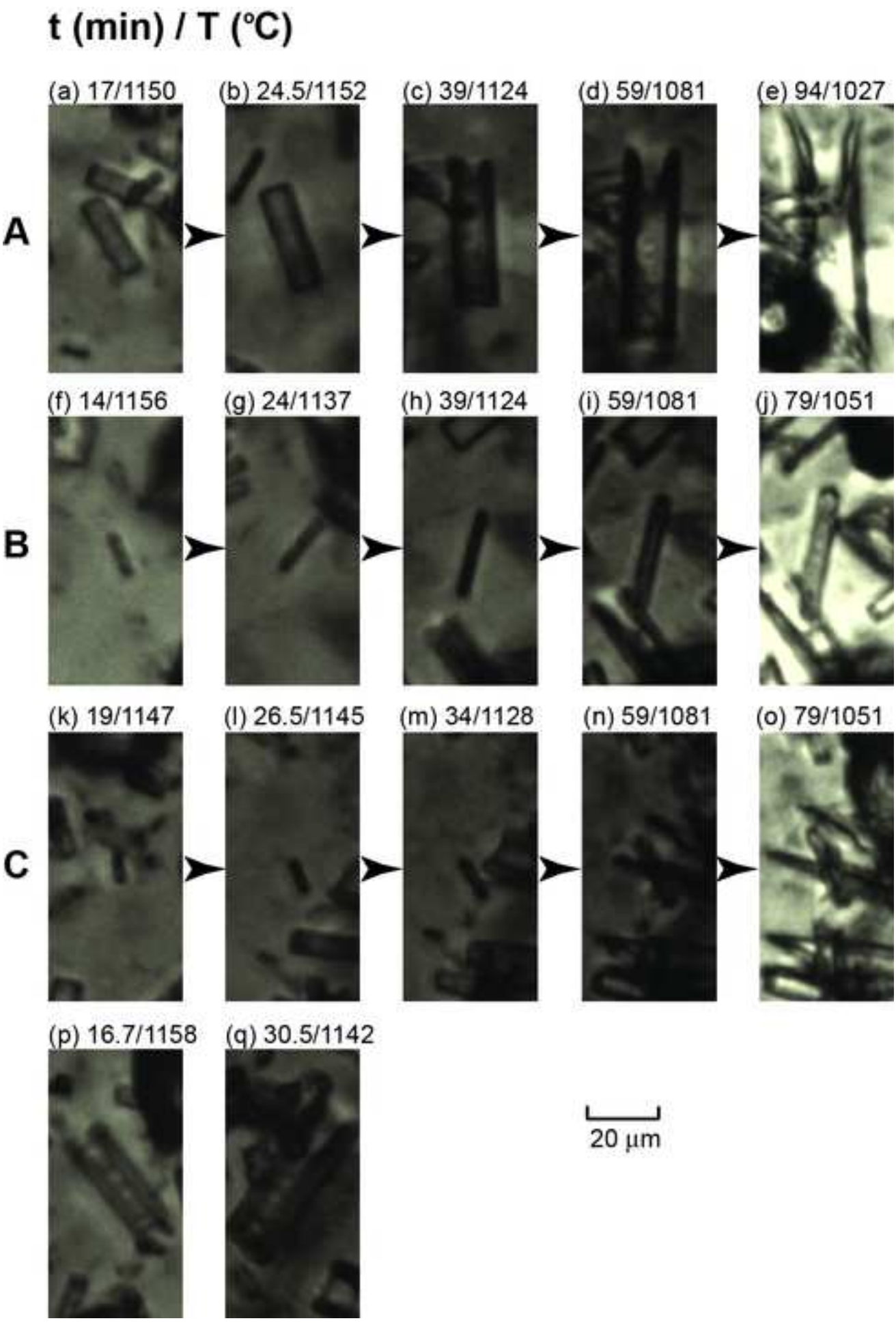

Figure4
Click here to download high resolution image

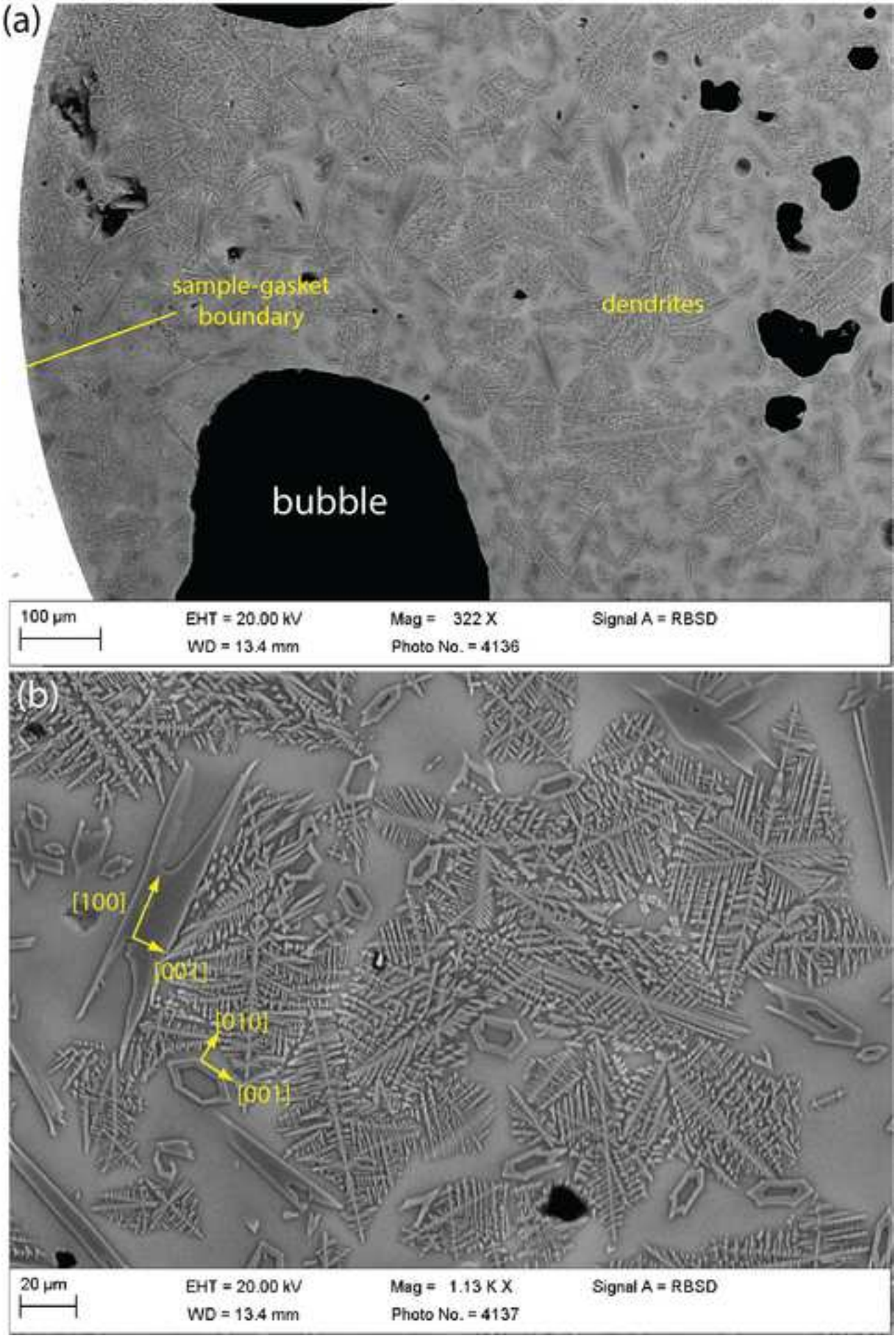

Figure5
Click here to download high resolution image

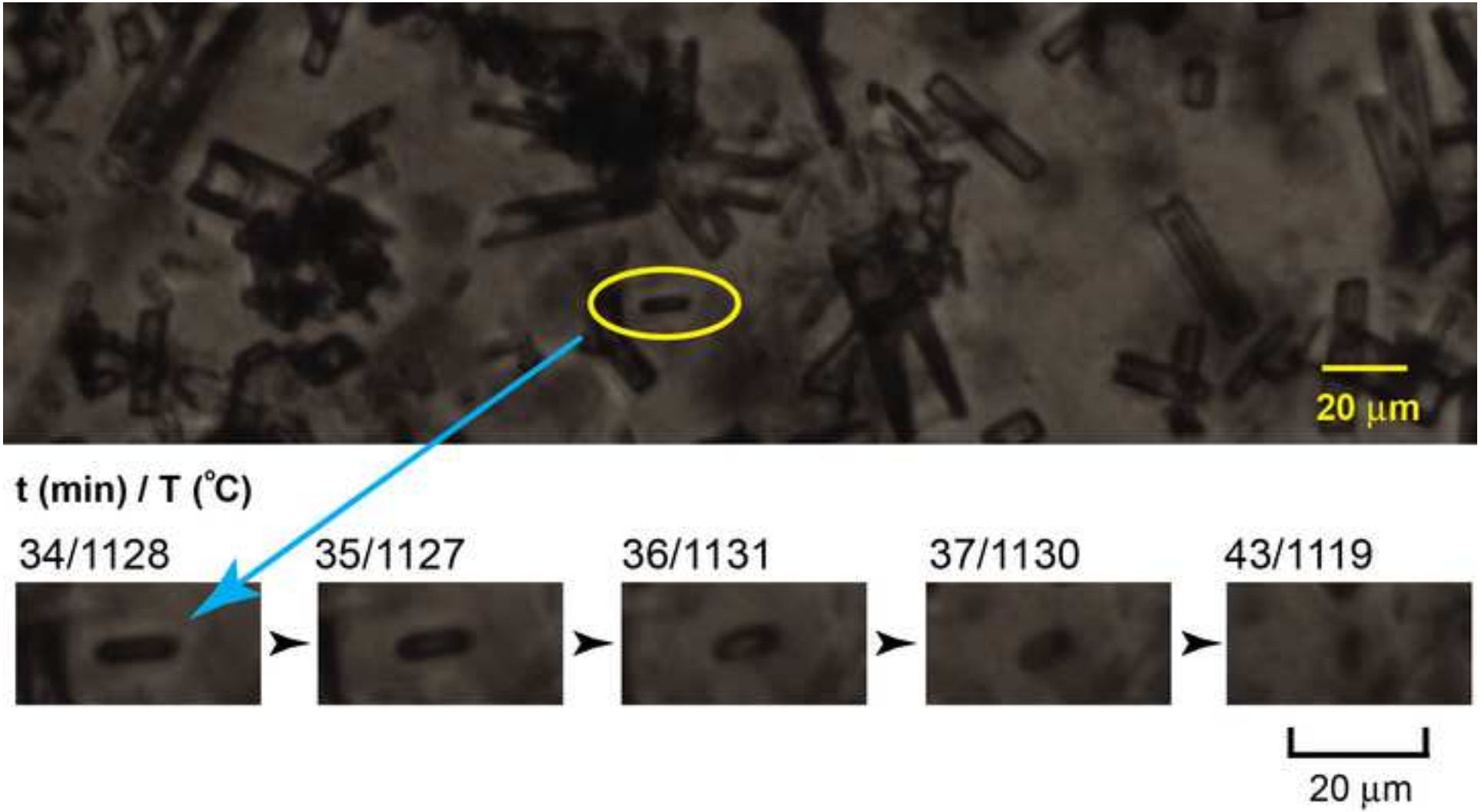

Figure6
Click here to download high resolution image

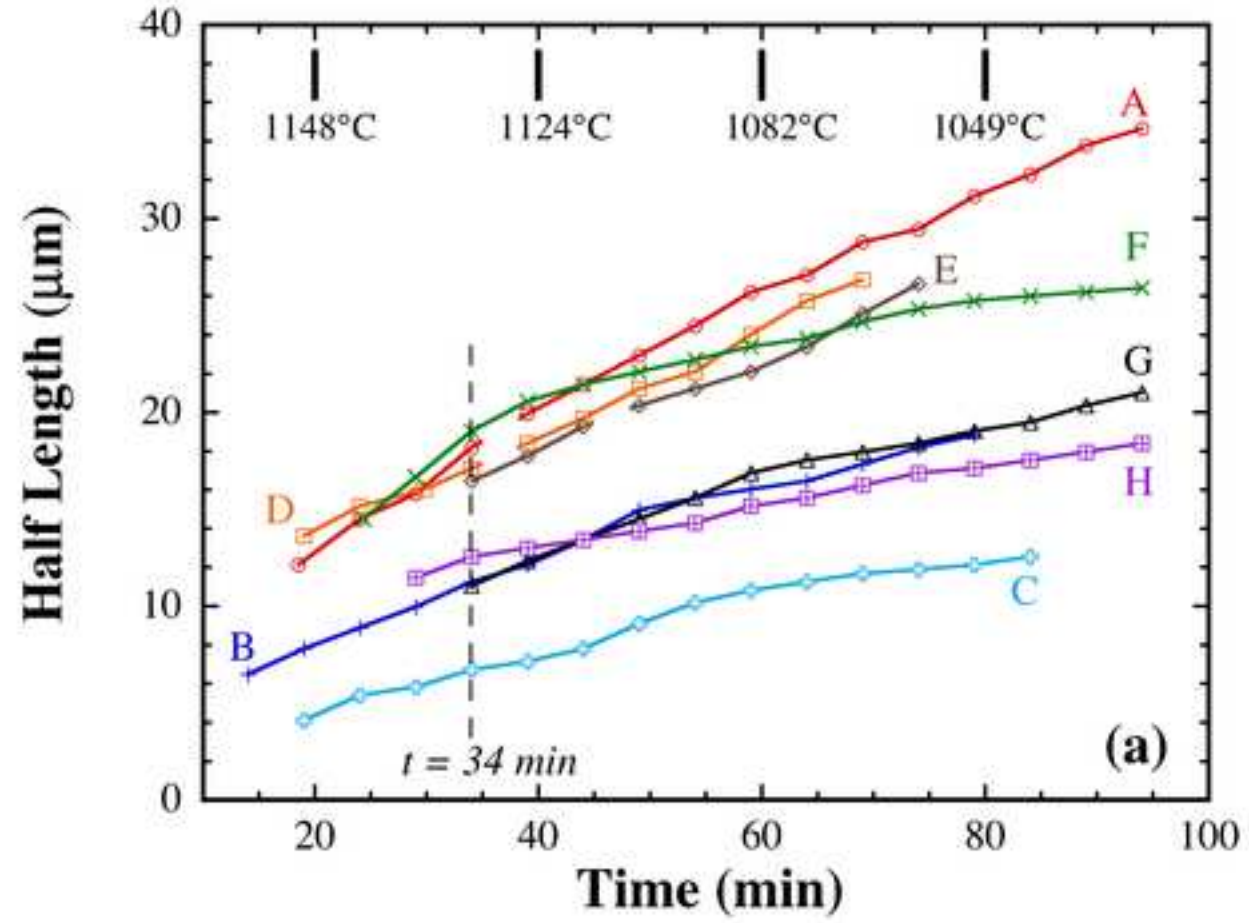

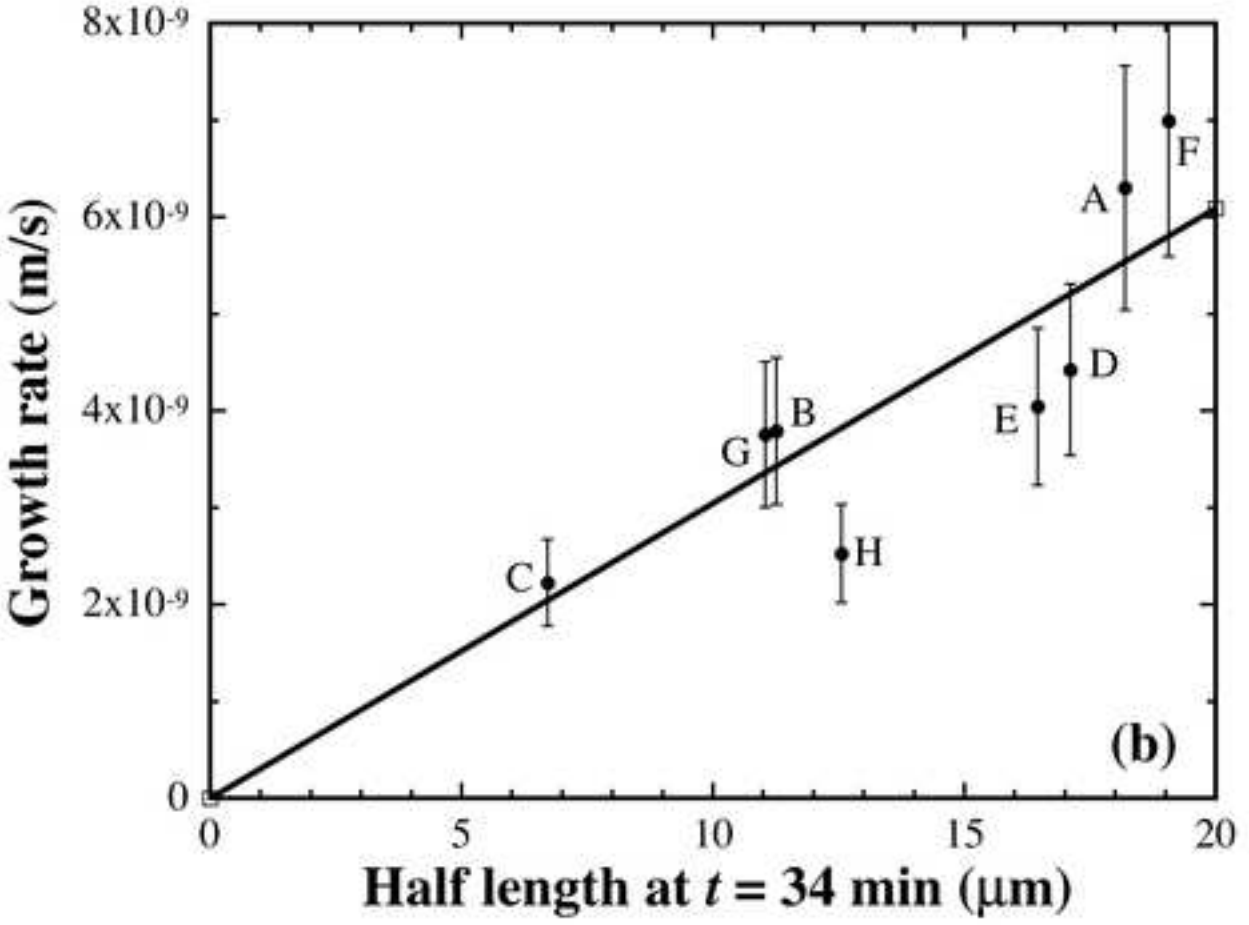

Figure7
Click here to download high resolution image

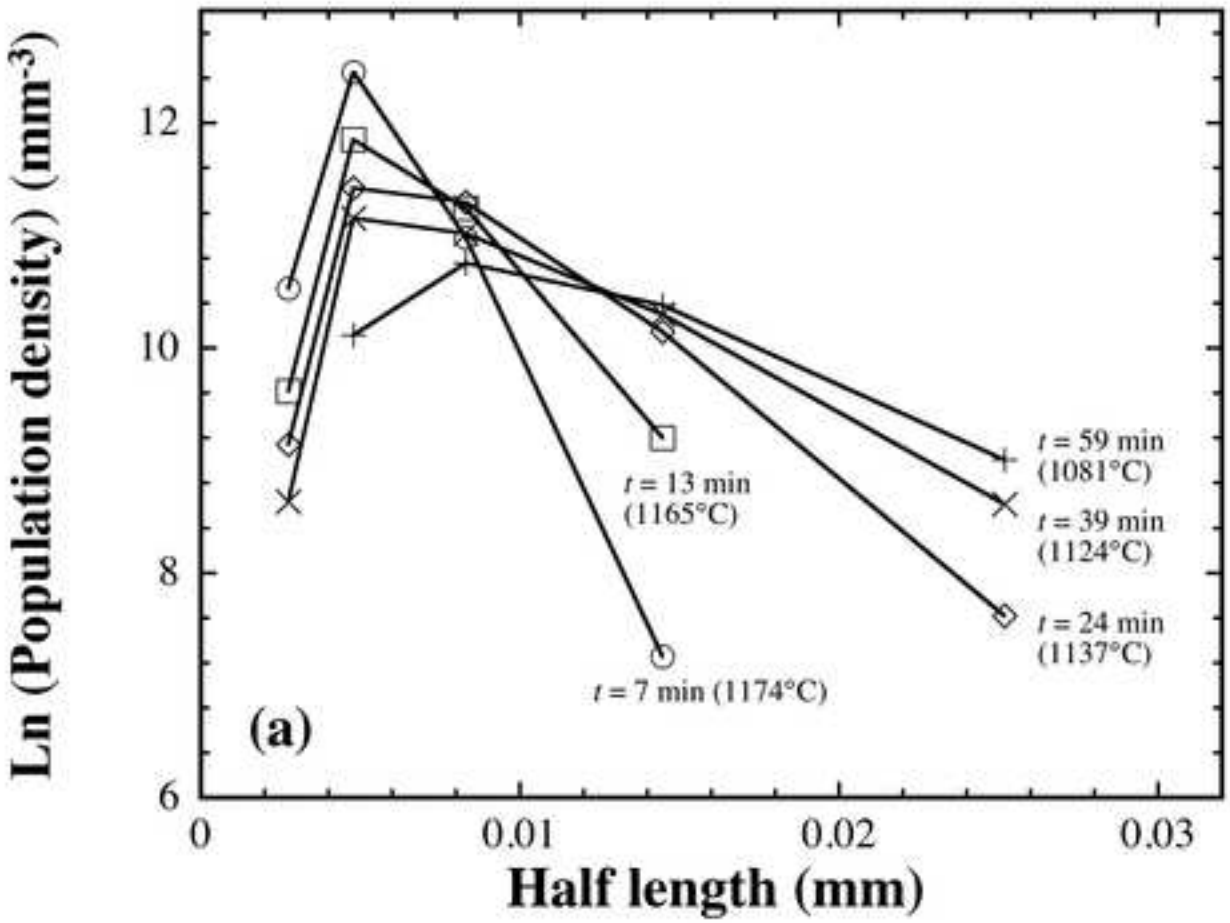

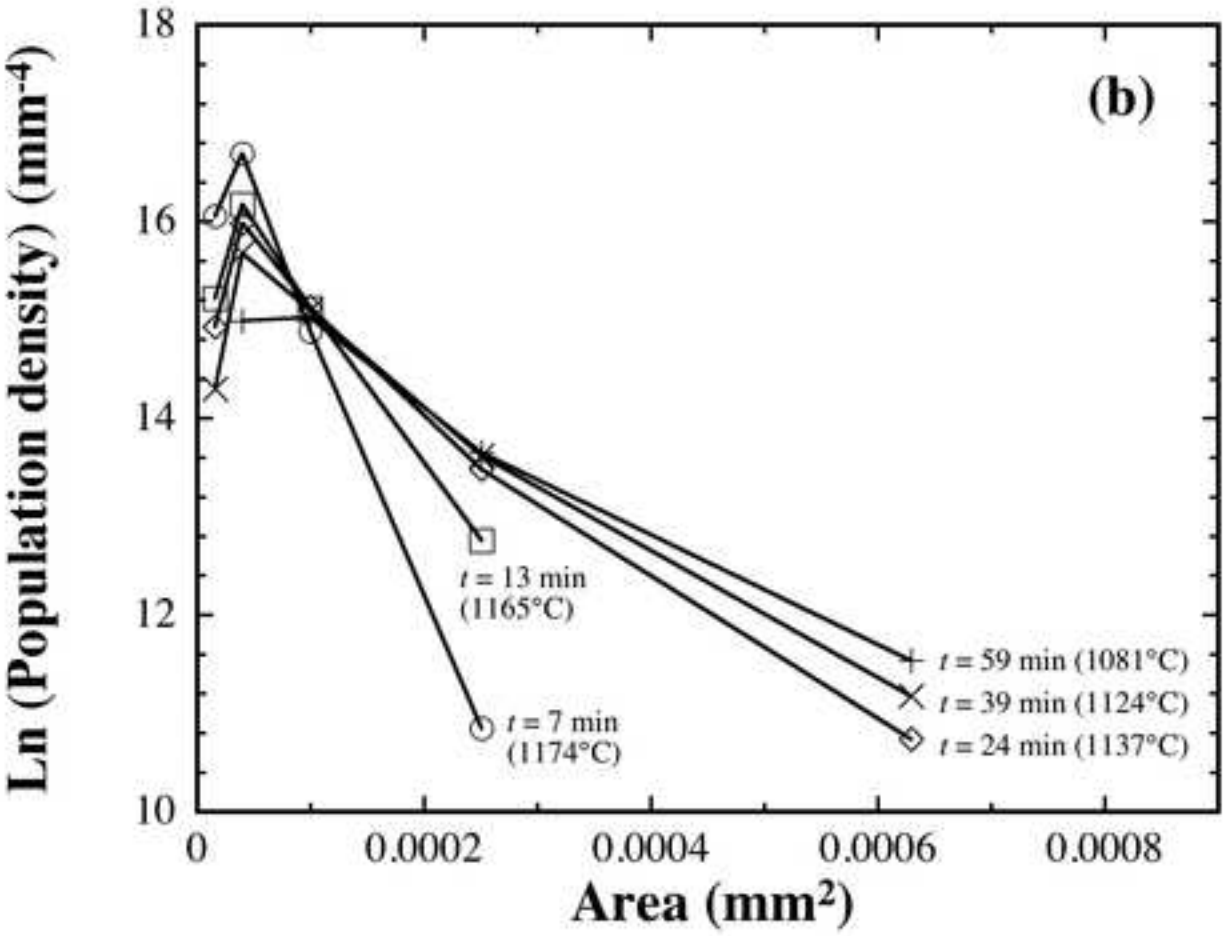

Figure8
Click here to download high resolution image

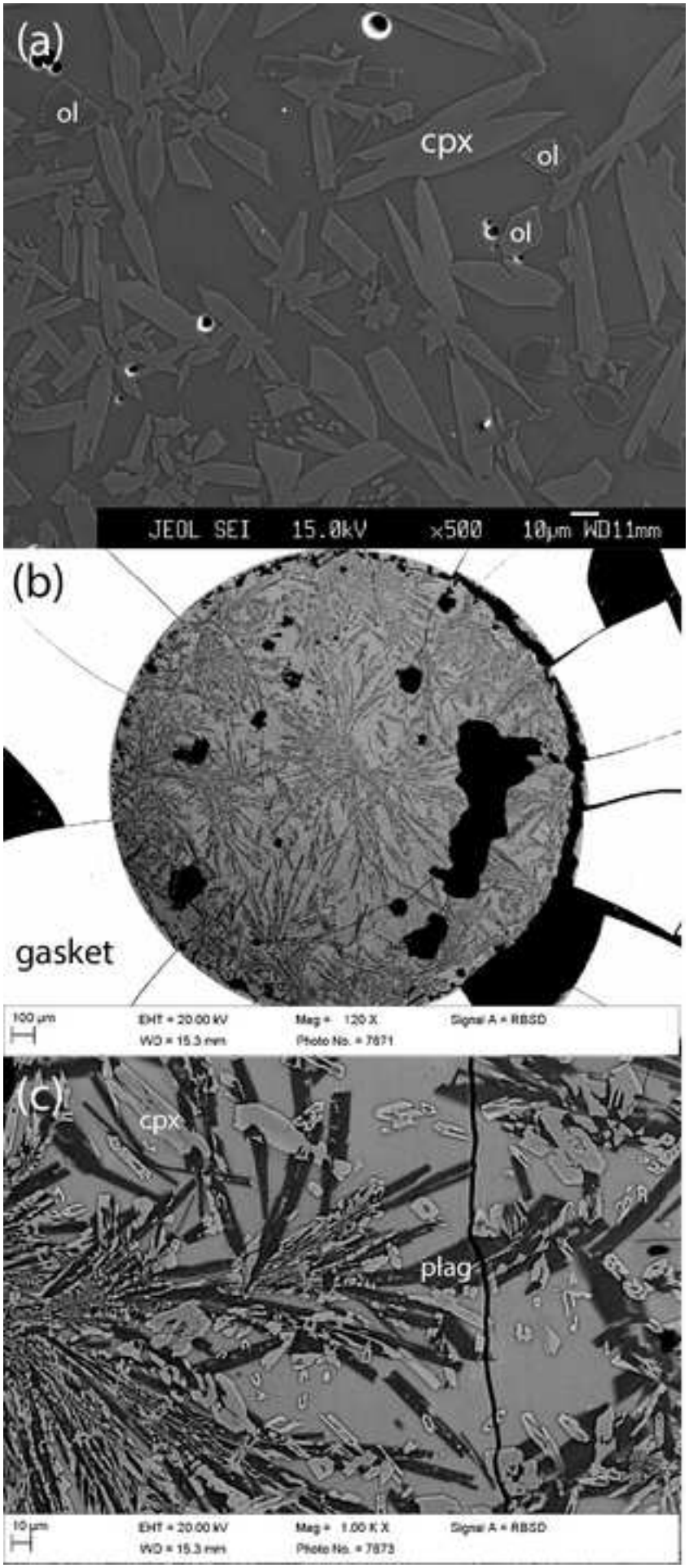

Figure9
Click here to download high resolution image

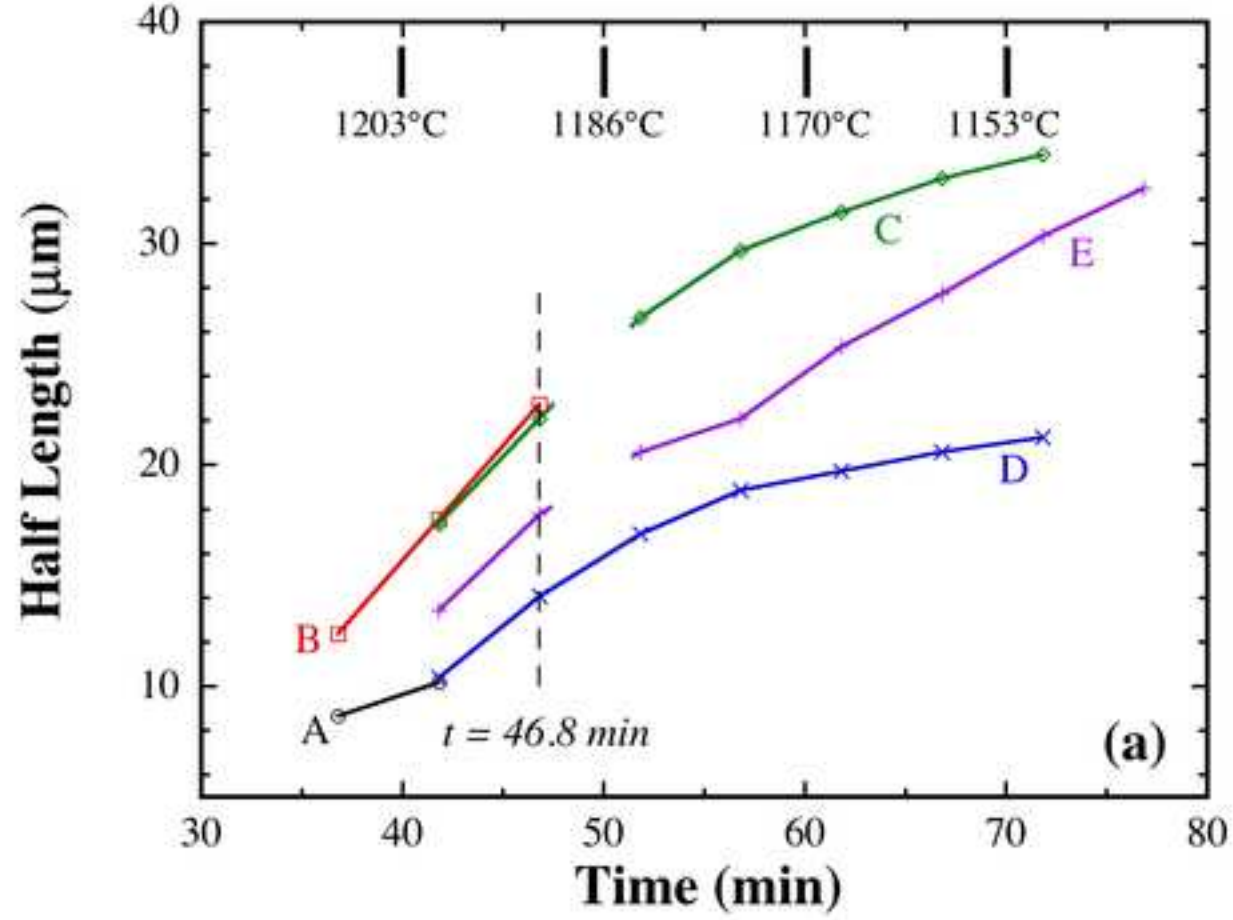

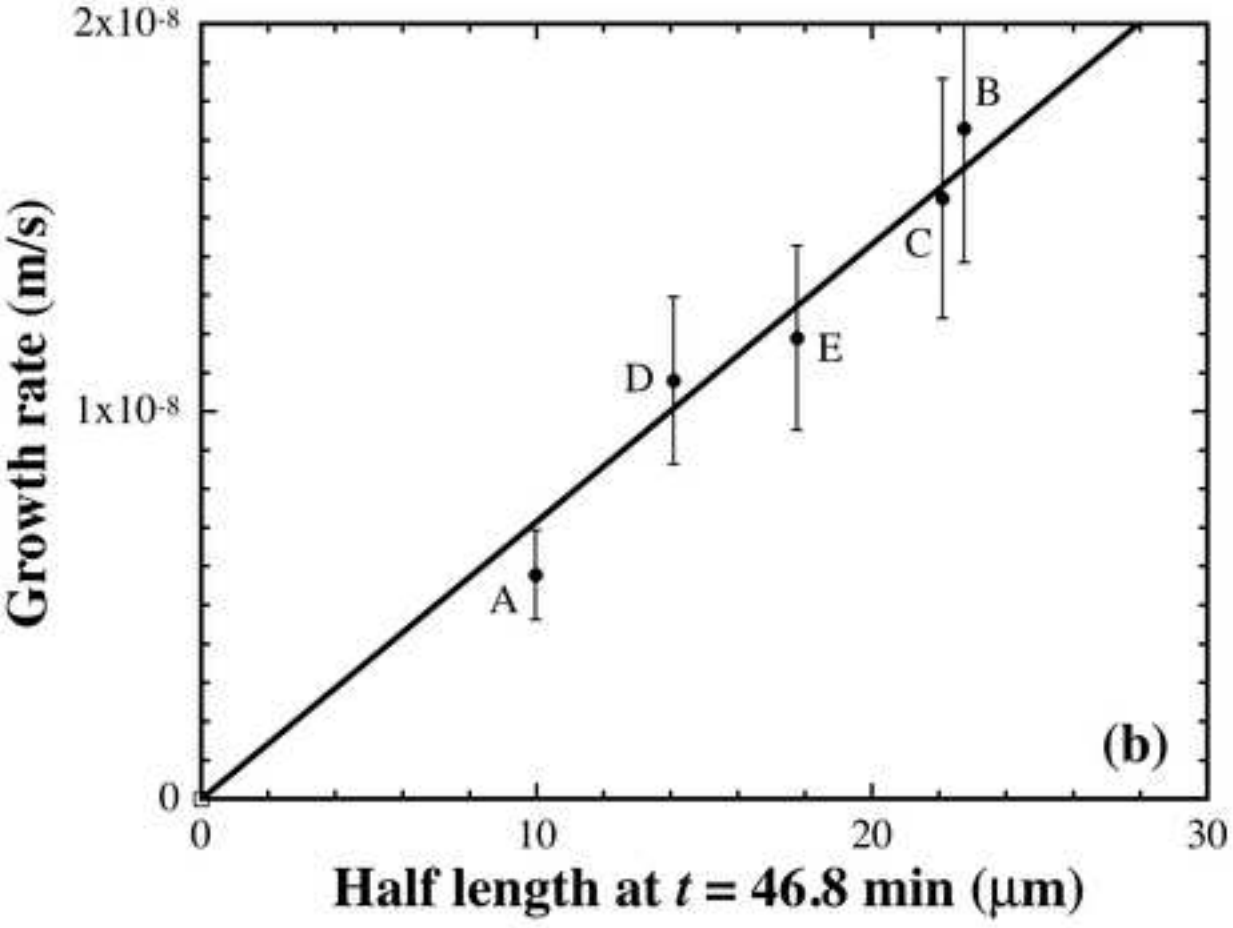

Figure10
Click here to download high resolution image

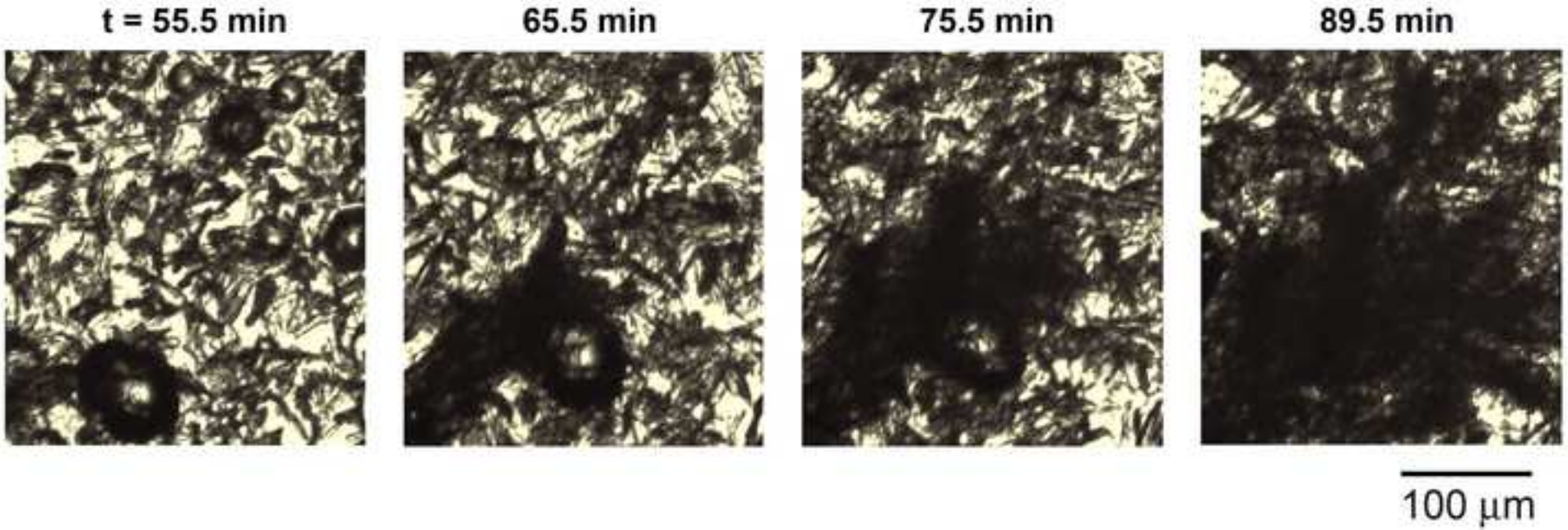

Figure11
Click here to download high resolution image

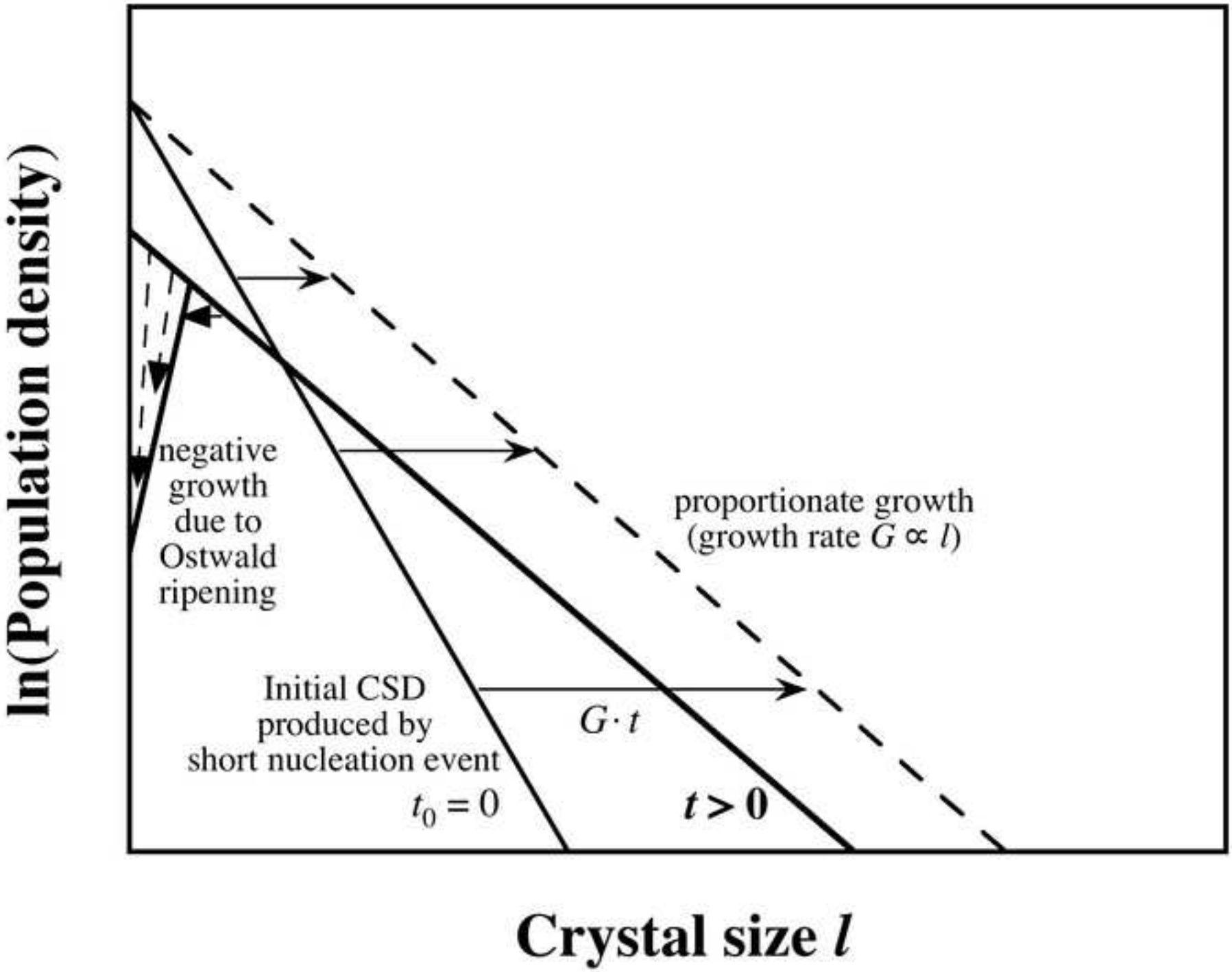

Table
Click here to download Table: Table.doc

Table 1 Composition of glasses and minerals in wt%

	SiO_2	TiO_2	Al_2O_3	FeO	MnO	MgO	CaO	Na_2O	K_2O	total
PST-9[1]	49.40	0.79	15.75	7.67	0.15	7.96	12.73	2.27	1.85	98.57
Bas[2]	52.29	0.85	16.29		7.81	7.53	10.24	3.15	2.21	100.37
Run# Bas11										
Olivine[3]	40.19				14.51	45.11	0.65			100.46
Melt[4]	53.94	1.00	18.56		6.72	2.39	11.94	3.03	2.51	100.09
Ol+Melt[5]	52.29	0.88	16.33		7.65	7.52	10.59	2.67	2.21	
Run# Bas14										
Cpx	49.59	1.36	8.23	0.02	8.07	16.11	17.19	0.22	0.04	100.83
Olivine	40.45				13.06	46.75	0.55			100.81
Melt	55.77	0.77	19.92	0.05	7.17	2.11	8.12	3.14	2.80	99.85
Run# Bas21										
Cpx	49.60	1.43	8.22	0.04	8.85	14.71	17.67	0.27	0.10	100.89
Plagioclase	53.48	0.17	28.16	0.01	1.31	0.52	11.95	3.92	1.06	100.58
Olivine	40.30				24.04	35.21	0.92			100.47
Melt	54.20	1.06	17.76	0.05	9.53	3.32	6.98	3.27	4.06	100.23

[1]A golden pumice from Stromboli volcano, containing also 0.43 wt% P_2O_5 (Pichavant et al. 2011), served as the target composition for glass synthesis.
[2]The starting synthetic glass for crystallization experiments.
[3]Olivine composition corresponds to $(Mg_{0.838}Mn_{0.153}Ca_{0.009})_2SiO_4$.
[4]Far-field melt (i.e., melt at some distance away from olivine crystals).
[5]Composition corresponding to 12 wt% olivine and 88 wt% far-field melt.

Table 2 Texture analyses of 5 snapshots in Run# Bas11

Time[1] (min)	*T* (°C)	Crystal density (counts/mm^2)	Max. crystal area (μm^2)	Max. crystal length (μm)	Crystal abundance (vol.%)
7	1174	993	221	12	4.7
13	1165	807	359	17	5.7
24	1137	841	609	27	8.6
39	1124	771	893	31	9.9
59	1081	638	865	32	10.5

[1]Elapsed time since a short nucleation event occurring at ~1048°C during heating.

Electronic supplementary material

Click here to download Electronic supplementary material: Supplementary material.doc

Movie A1

Click here to download Video: Movie_A1(Bas11).mpg

Movie A2

Click here to download Video: Movie_A2(Bas12).mpg

Movie A3

Click here to download Video: Movie_A3(Bas14).mpg

Movie A4

Click here to download Video: Movie_A4(Bas21).mpg